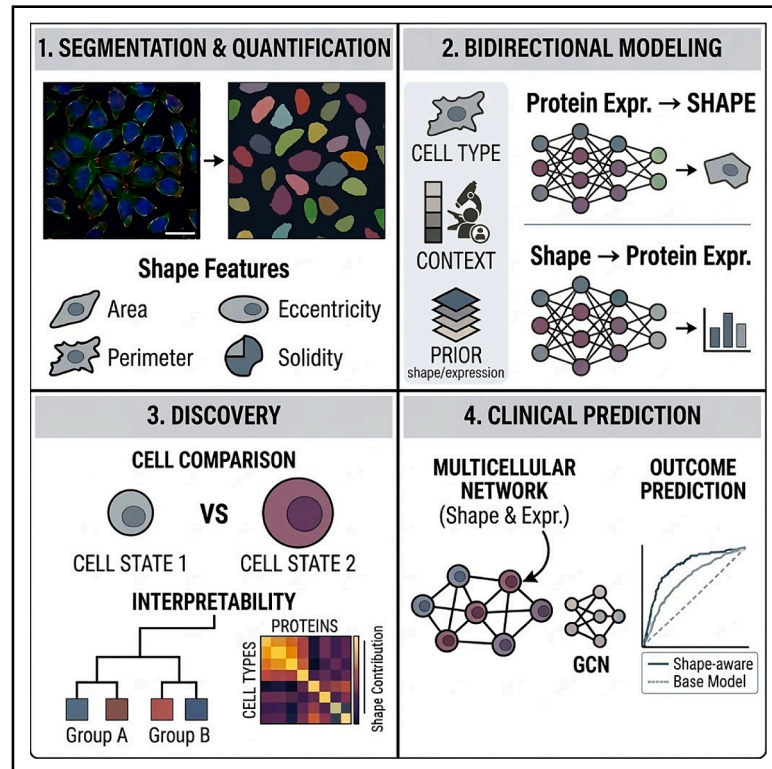


# Data modeling the interplay between single-cell shape, single-cell protein expression, and tissue state

## Graphical abstract



## Authors

Yuval Tamir, Yuval Bussi, Claudia Owczarek, ..., Maddy Parsons, Leeat Keren, Assaf Zaritsky

## Correspondence

assafzar@gmail.com

## In brief

Tamir et al. demonstrate that a cell's shape is coupled with its molecular profile in human tissues. By combining multiplexed imaging with machine learning, they show that shape explains protein variations within specific cell types, enabling the discovery of new cell subtypes and improving the accuracy of disease state characterization.

## Highlights

- Machine learning reveals a universal link between cell shape and protein expression
- Single-cell shape predicts protein levels better than cell type alone
- Shape features identify p53-positive tumor subpopulations across cancers
- Integrating cell shape improves graph-based predictions of clinical tissue states

## Report

# Data modeling the interplay between single-cell shape, single-cell protein expression, and tissue state

Yuval Tamir,<sup>1</sup> Yuval Bussi,<sup>2,3</sup> Claudia Owczarek,<sup>4</sup> Luciana Luque,<sup>5</sup> Giuseppe Torrisi,<sup>5</sup> Leor Ariel Rose,<sup>1</sup> Orit Kliper-Gross,<sup>1</sup> Linus Schumacher,<sup>5</sup> Maddy Parsons,<sup>4</sup> Leeat Keren,<sup>2</sup> and Assaf Zaritsky<sup>1,6,\*</sup>

<sup>1</sup>Institute for Interdisciplinary Computational Science, Stein Faculty of Computer and Information Science, Ben-Gurion University of the Negev, Beer-Sheva 84105, Israel

<sup>2</sup>Department of Molecular Cell Biology, Weizmann Institute of Science, Rehovot 761001, Israel

<sup>3</sup>Department of Mathematics and Computer Science, Weizmann Institute of Science, Rehovot 761001, Israel

<sup>4</sup>Randall Centre for Cell and Molecular Biophysics, King's College London, Guy's Campus, London SE1 1UL, UK

<sup>5</sup>Centre for Regenerative Medicine, University of Edinburgh, Edinburgh, UK

<sup>6</sup>Lead contact

\*Correspondence: [assafzar@gmail.com](mailto:assafzar@gmail.com)

<https://doi.org/10.1016/j.crmeth.2026.101463>

**MOTIVATION** Cell shape is a key indicator of physiological state, yet the precise dependencies between shape and molecular profiles have remained largely unquantified *in situ*. We developed this method to systematically model these interactions, providing a scalable approach to identify how shape heterogeneity reflects specific protein variations. While our method reveals robust predictive links, it is currently limited by 2D imaging constraints and the inability to infer direct causality between shape and expression. Nevertheless, this approach offers a high-throughput means to discover clinically relevant cell subpopulations and refine our understanding of tissue-scale organization.

## SUMMARY

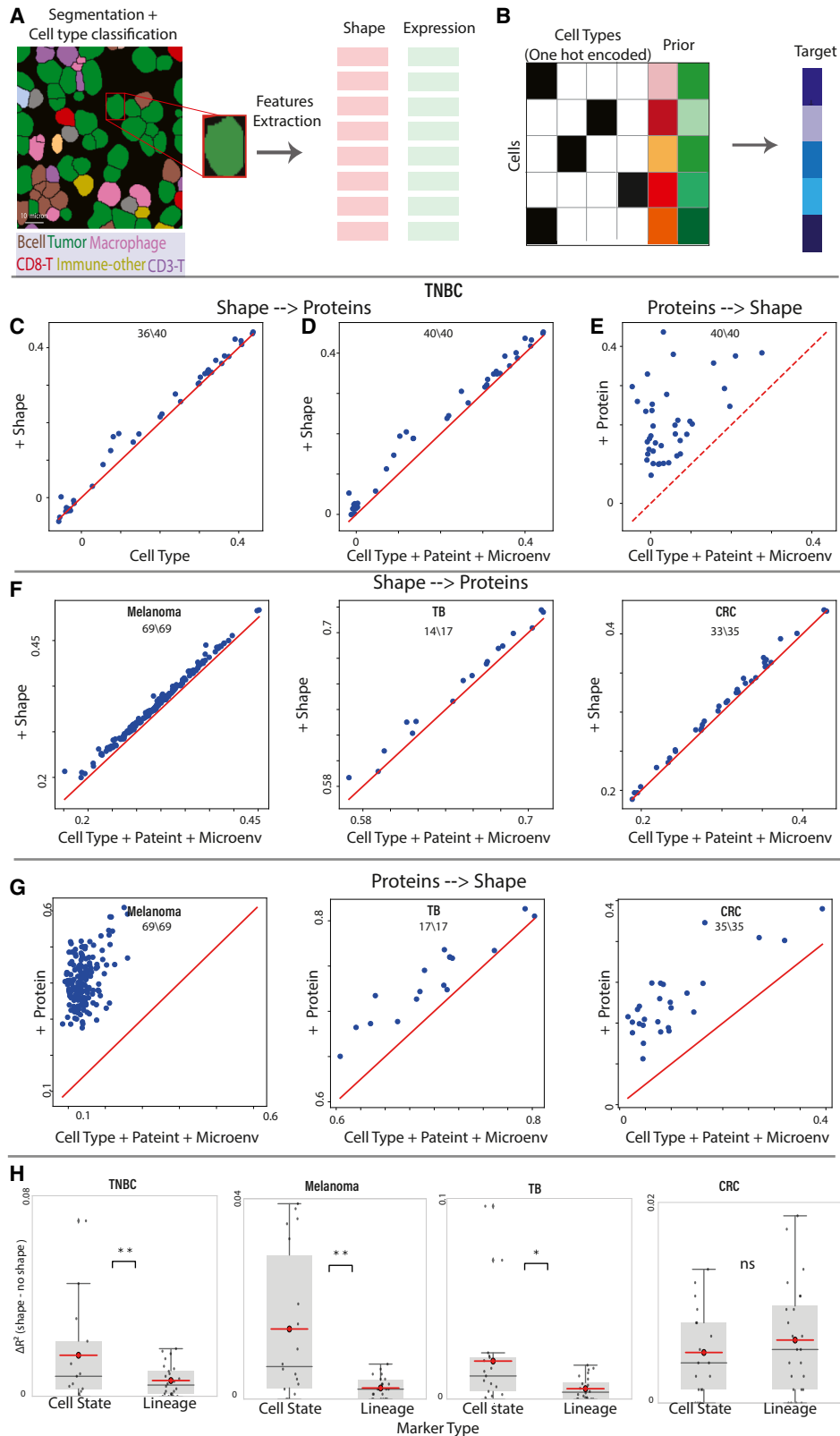
While cell shape fundamentally governs tissue function, the underlying links between single-cell shape and protein expression have been difficult to resolve due to limitations in imaging multiplexing and population averaging. Here, we use multiplexed imaging and machine learning to investigate the coupling of cell shape and protein expression in heterogeneous human tissues. Our analysis establishes a universal, bi-directional link between a cell's shape and its protein expression across cell types, diseases, and disease states, amplified for cell state markers. Machine learning interpretability shows that shape features can potentially generate hypotheses of protein functions. Screening all protein-cell type pairs identified a subpopulation of large, p53-positive tumor cells across two cancers. Shape properties further enhanced graph neural network disease state prediction. Our results open the door to unraveling the intricate connections between protein expression, cell shape, tissue organization, and tissue state in a physiological context.

## INTRODUCTION

Since the early days of Rudolf Virchow, and for over 200 years, pathologists have been using microscopes to observe tissue architectural patterns, cellular rearrangements, cell and nuclear shape, and intracellular organization to diagnose and make treatment decisions. Throughout evolution, diverse cell shapes and intracellular organization, broadly termed *cell morphology*, enable diverse cellular functions.<sup>1,2</sup> Single-cell morphology, even when considering a single cell type, encodes information related to gene expression patterns,<sup>3</sup>

signaling,<sup>4</sup> functional states,<sup>5</sup> dynamics,<sup>6</sup> and even metastatic potential.<sup>7</sup> Accordingly, single-cell morphology, and specifically cell shape,<sup>8,9</sup> are quantitative readouts extensively used for applications of high-content cell imaging, such as systematic morphological profiling<sup>4,10,11</sup> and drug screening.<sup>12,13</sup>

Recent spatial single-cell imaging technologies, such as multiplexed ion beam imaging by time-of-flight (MIBI-TOF)<sup>14</sup> or Co-Detection-by-inDEXing (CODEX),<sup>15</sup> enable multiplexed imaging of dozens of proteins at single-cell resolution within tissue sections. These technologies enable the resolution of



(legend on next page)

different cell types and their spatial organization in their native context within the tissue and allow researchers to ask how the tissue's spatial organization influences function and/or pathology. For example, several recent studies have demonstrated that the cellular local neighborhood context is linked to a single cell's protein expression profile<sup>16</sup> and even to the disease state.<sup>17</sup> These spatial single-cell imaging technologies enable the systematic study of the fundamental relationships between cell shape and protein expression in a physiological context, *in situ*.

Here, we established that single-cell shape and protein expression are inter-linked in disease-related tissue sections. Specifically, we show that cell shape explains some of the within-cell type variations in protein expression and vice versa in a human cohort of triple-negative breast cancer (TNBC) tissue sections. This link between single-cell shape and protein expression is further confirmed for independent patient cohorts of tuberculosis (TB), colorectal cancer (CRC), melanoma, and head and neck cancer (HNC) and is amplified for cell state markers. By screening the links between cell shape and protein expression in all pairs consisting of one protein and one cell type in the TNBC cohort, we identified enrichment of the protein p53 in larger tumor cells. This relationship between p53 and tumor cell size was confirmed in another TNBC cohort that was acquired in a different hospital with a different technology. Finally, we showed that the inclusion of single-cell shape properties improves disease state prediction by graph neural networks that rely on the cells' protein expression and their spatial organization in the TNBC and HNC cohorts. Altogether, our results indicate that cell shape contains information regarding within-cell type protein expression variations and suggest that this information can be used to identify cell subtypes and cell states, and to enhance the prediction of disease state in heterogeneous tissue sections.

## RESULTS

### Cell shape heterogeneity in TNBC

We reanalyzed data from a human TNBC cohort, previously collected by MIBI-TOF, consisting of 40 tissue sections from different patients, depicting 36 protein channels at subcellular resolution.<sup>18</sup> Using the single-cell segmentation masks,<sup>19</sup> we extracted 12 standard single-cell shape features (Table S1), 36 single-cell normalized protein expression values, and expert-validated annotations categorized every cell into one of 16 different cell types (Figure 1A). Using the single-cell type annotations, we analyzed shape features across the different cell types. Visual assessment showed heterogeneity in cell shapes, even within the same cell type (Figure 1A). Systematically associating cell shape with cell type showed that tumor cells were the largest and the most heterogeneous cell type, macrophages had the lowest convex hull-to-area ratio, and T regulatory cells were the most homogeneous in terms of size (Figures S1 and S2). However, systematic machine learning analysis was not able to effectively classify the cell types based on their 12-dimensional shape features (Figure S3). These results imply that cell shape variability between patients and within cell types induces only weak associations between cell type and cell shape, indicating that cell shape does not contain strong discriminative information regarding cell type, at least at the crude spatial resolution of 0.5  $\mu\text{m}$  per pixel, which is standard in spatial single-cell assays.

### Within-cell type association of single-cell shape and protein expression

Most of MIBI-TOF's 36 multiplexed protein antibodies are selected to determine cell type. Thus, the main source of variability in protein expression between cells is attributed to cell type. The residual variation in protein expression within a cell

#### Figure 1. Single-cell shape and protein expression are associated

(A) Depiction of the extraction of cell shape features and protein expression. The raw multiplexed images were segmented into single cells, and each cell was categorized according to its cell type. Single-cell shape features were extracted from the single-cell segmentation masks, and single-cell protein expression was extracted from the segmentation masks and multiplexed images. Scale bar: 10  $\mu\text{m}$ .

(B) To isolate and quantify the influence of a prior (cell shape or protein expression) on the prediction of a single-cell target (protein expression or cell shape, respectively), we compared the performance of prior-aware model to models without priors. The schematic depicts an example of a single-cell representation. Each row represents a cell, where the cell type is encoded via one-hot encoding and the prior (color) can be concatenated to it for a prior-aware model.

(C–G) Shape-aware (C, D, F) and protein expression-aware (E, G) models surpassed models trained without the corresponding prior in predicting single-cell protein expression or cell shape, respectively. Each data point represents a patient, showing the adjusted  $R^2$  between models without prior ( $x$  axis) and the corresponding prior-aware models ( $y$  axis). Data points above the diagonal  $y = x$  are those patients whose model predictions were improved by inclusion of the prior. Statistical significance was calculated via Wilcoxon signed-rank test, rejecting the null hypothesis that the difference between adjusted  $R^2$  value is distributed around 0.

(C–E) Patients with TNBC. (C) Shape prior contributes to a model trained with cell type in 36/40 patients ( $p < 0.0001$ ). (D) Shape prior contributes to a model trained with cell type, patient, and cell microenvironment composition in 40/40 patients ( $p < 0.0001$ ). (E) Protein expression prior contributes to a model trained with cell type, patient, and cell microenvironment composition in 40/40 patients ( $p < 0.0001$ ). (F) Shape-aware models surpassed models trained with cell type, patient, and cell microenvironment composition in predicting single-cell protein expression across diseases for 69/69 patients with melanoma ( $p < 0.0001$ ), 14/17 patients with tuberculosis (TB) ( $p < 0.001$ ), and 33/35 patients with colorectal cancer (CRC) ( $p < 0.0001$ ). (G) Protein expression-aware models surpassed models trained with cell type, patient, and cell microenvironment composition in predicting single-cell shape across additional diseases for 69/69 patients with melanoma ( $p < 0.0001$ ), 17/17 patients with TB ( $p < 0.0001$ ), and 35/35 patients with CRC ( $p < 0.0001$ ).

(H) Inclusion of cell-shape priors for cell state versus lineage markers across datasets. Boxplots show the distribution of  $\Delta$ adjusted  $R^2$  (i.e., prediction improvement by incorporating cell-shape priors) for cell-state markers versus lineage markers across the TNBC, melanoma, TB, and CRC cohorts. Red (black) lines mark the median (mean), respectively. Boxes represent the interquartile range (25th–75th percentile); whiskers extend to 1.5 $\times$  the IQR; and individual data points are overlaid as dots. Statistical comparisons were performed using  $t$  tests between  $\Delta$ adjusted  $R^2$  of cell state versus lineage marker groups within each dataset. The contribution of shape priors to the prediction of cell-state markers was enhanced in TNBC (\*\* $p < 0.001$ ), melanoma (\*\* $p < 0.001$ ), and TB ( $p < 0.05$ ) but not significant (ns) for CRC.

See also Figures S1–S7.

type is commonly attributed to cell cycle states,<sup>20</sup> microenvironment,<sup>16,21</sup> and more refined cell state characterization.<sup>22</sup> Given the high variation in cell shapes within the same cell type, we hypothesized that some of the variations in single-cell normalized protein expression per area unit (from here on referred to as “protein expression”) within the same cell type can be related to cell shape, and vice versa—that some of the variation in cell shape can be related to protein expression. We tested this hypothesis by using machine learning to predict a cell’s protein expression given its cell shape, and to predict a cell’s shape given its protein expression (Figure 1B). In this context, cell shape or protein expression are termed the “prior”. First, we assessed whether the inclusion of cell shape features (i.e., shape-aware model) contributed to the prediction of protein expression beyond a baseline model defined by cell type alone (STAR Methods). Specifically, for each model, we calculated the adjusted coefficient of determination (adjusted  $R^2$ ), a standard metric for assessing the accuracy of a regression task, and then used this metric to compare models with versus without the cell shape priors. Shape-aware models surpassed the baseline model. Specifically, a shape-aware fully connected deep neural network (DNN) model surpassed the baseline model in 36 out of the 40 patients’ tissue sections, underscoring that cell shape encodes some of the variation in protein expression beyond the information encoded by cell type alone (Figure 1C). The DNN model also surpassed other shape-aware linear models (Figure S4A). This improvement was not due to increased model complexity from the inclusion of cell shape, as demonstrated by the reduced capacity to predict protein expression after shuffling shape features between cells (Figure S4B). To exclude the possibility that this contribution of cell shape to the prediction of protein expression was confounded by inter-patient variability, we validated that cell shape contributes to a model conditioned on both cell type and patient (STAR Methods). The patient- and shape-aware model surpassed the model without shape information in 35 out of 40 patients (Figure S4C). To exclude the possibility that the residual protein expression explained by cell shape was confounded by the cell microenvironment, we validated that inclusion of cell shape surpassed a model that was trained with cell type, patient, and cell microenvironment composition, where microenvironment composition was defined as all cells that appear within a radius of 70  $\mu\text{m}$ <sup>16</sup> (STAR Methods). The cell type-, patient-, microenvironment-, and shape-aware model surpassed the model without shape information in all 40 patients (Figure 1D). To quantify how much deterioration in cell segmentation can reduce the contribution of cell shape to the prediction of protein expression, we measured the effect of reduced resolution by downscaling the segmentation masks (Figure S5A) and measured the effect of segmentation errors by gradually introducing measurement noise to the (segmentation-derived) cell shape measurements (Figure S5B). Both sensitivity analyses showed a gradual decay in the contribution of cell shape to the prediction of protein expression, with contribution still measurable even at high levels of segmentation noise, suggesting robustness to small variations in segmentation quality.

Having established that cell shape contributes to the prediction of protein expression beyond cell type in patients with

TNBC, we next investigated the opposite direction to determine whether protein expression provides information beyond cell type for cell shape prediction. Similarly to the previous analysis, we trained a fully connected neural network model to predict the 12 cell shape features using cell type and protein expression as a prior and compared its performance to a baseline model that was conditioned on cell type alone. The protein expression-aware model surpassed the baseline cell shape model with an average  $\Delta$ adjusted  $R^2$  of  $\sim 10\%$ . This contribution of protein expression to cell shape prediction was not confounded by the patient nor by the cellular microenvironment composition and was measured for all 40 patients (Figures 1E, S1D, and S1E; Table S2). These results indicate that protein expression encodes information about cell shape beyond what is captured by cell type in patients with TNBC.

Our analysis of intra-cell type variations suggests an association between cell shape and protein expression in TNBC tumors. To assess the generalizability of these findings, we repeated the same analysis on three additional datasets: a public MIBI-TOF TB dataset,<sup>23</sup> a public CODEX CRC dataset,<sup>24</sup> and a MIBI-TOF melanoma dataset<sup>25</sup> (STAR Methods). Across all datasets, shape- and protein-aware models surpassed their corresponding baseline models, cumulatively for 156/161 ( $\sim 96\%$ ) and 161/161 ( $\sim 100\%$ ) of the patients, correspondingly (Figures 1F, 1G, and S6; Table S2). These results establish an association between cell shape and protein expression that generalizes across multiple human diseases.

For all diseases and all models, cell shape showed a modest contribution to the prediction of protein expression, with an average  $\Delta$ adjusted  $R^2$  of  $\sim 1\%$ – $2\%$ , that appeared consistently in over 95% of the patients (Table S2). This magnitude of improvement agrees with a previous study that explored the contribution of the cellular microenvironment to the prediction of single-cell protein expression,<sup>16</sup> aligning with the understanding that the most dominant source of variability in protein expression is cell type. Importantly, most proteins in the TNBC panel were selected to infer cell type (termed “lineage markers”) and thus were not necessarily expected to associate with within-cell type cell shape variability. Since cell shape was previously associated with cell state markers,<sup>3</sup> we specifically assessed and reported the contribution of cell shape to the prediction of the subset of cell state markers using the cell type-, patient-, and microenvironment-aware models. The inclusion of cell shape improved the prediction of cell state markers more than the prediction of lineage markers across diseases (Figure 1H) and across 152/161 ( $\sim 94\%$ ) of patients (Figure S7). Several cell state proteins consistently showed shape-aware improved prediction across diseases, including DNA content (4/4 diseases with this marker), histones (2/2 diseases), PD-1 (3/4 diseases), FoxP3 (3/3 diseases), Ki67 (4/4 diseases), human leukocyte antigen DR (HLA-DR) (2/2 diseases), and p53 (2/2 diseases). The most prominent improvement of roughly 5%–12% by shape-aware models was reported for DNA and histone markers (Figure S7).

### Shape feature importance clusters according to proteins function

Cell shape was found to contribute to protein expression prediction, but it was not clear which shape features were most

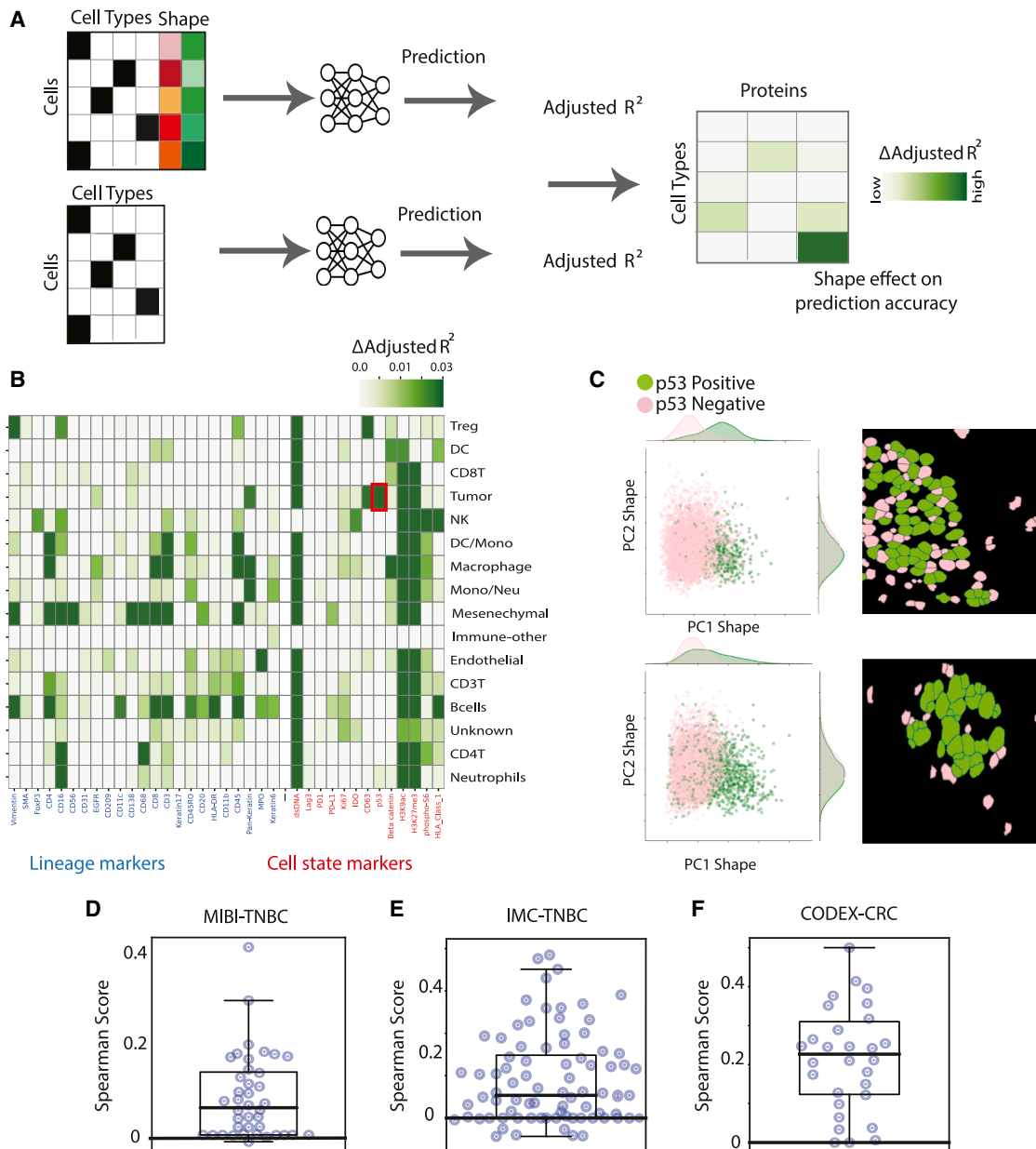


**Figure 2. Screening for shape-dependent protein expression**

(A) For each pair of cell type and protein expression, we calculated the change in adjusted  $R^2$  values between the observed and predicted outcomes of the shape-aware model relative to the baseline. These pairs define the  $\Delta$ adjusted  $R^2$  matrix, which measures and visualizes the contribution of cell shape to the prediction of protein expression (x axis) in the context of a cell type (y axis).

(B) Visualization of the  $\Delta$ adjusted  $R^2$  matrix computed by subtracting the baseline model's  $R^2$  scores from the shape-aware model's  $R^2$  scores. For visual clarity, only positive values (508/576) are displayed. The x axis represents the quantified proteins, and the y axis represents the annotated cell types. The red box emphasizes the shape-dependent improvement in tumor cells' p53 expression prediction.

(C) Representative examples of two patients (#28 top, #16 bottom) demonstrating the association between p53-positive/negative status (determined according to p53 expression, see STAR Methods) and cell shape. Left: Scatterplots of tumor cells' 2D shape-space principal component analysis (PCA) projection, with cells colored according to their p53-positive (green) or p53-negative (pink) status. A t test rejected the null hypothesis that the PC1 values are distributed around the same mean for both p53-positive and p53-negative cells, with a p value < 0.0001. Statistical significance was recorded in 16/20 patients that had sufficient cell count (>100) of p53-positive and p53-negative tumor cells (Figure S5). Right: representative segmented tumor cells from the corresponding patients show apparent qualitative shape difference between p53-positive (green) and p53-negative (pink) tumor cells.

(legend continued on next page)

influential in improving the predictions. To explain the predictions of the shape-aware model, we applied the SHapley Additive exPlanations (SHAP) interpretability method,<sup>26</sup> which assigns each feature an importance value for each prediction of our TNBC cell type- and shape-aware model. To specifically evaluate shape, we ignored the SHAP values attributed to the cell type feature, focusing on the SHAP values attributed to the 12 cell shape features, which we refer to as “shape influence signatures.” We aggregated these shape influence signatures for each protein and found that size-related features, such as perimeter and area, had the highest overall importance, while shape-related features, such as orientation, solidity, and eccentricity, were slightly less important for the model’s predictions across all protein targets (Figure S8A). We performed hierarchical clustering of the proteins according to their corresponding 12-dimensional shape influence signatures. This analysis identified clusters of proteins whose predictions were similarly influenced by cell shape (Figure S8B). One cluster included keratin-6, beta-catenin, keratin 17, and pan keratin, proteins that are known to be overexpressed in many cancers, including TNBC, and serve as potential diagnostic and prognostic markers.<sup>27–30</sup> A second cluster comprised H3K9ac, dsDNA, H3K27me3, Ki67, and phospho-S6, which includes nuclear cell status markers for proliferation (Ki67)<sup>31</sup> and histone modification markers (H3K27me3 and H3K9ac<sup>32</sup>). Zooming into the SHAP values of the individual proteins showed striking within-cluster similarities and between-cluster differences in these shape influence signatures (Figure S8C).

To examine the shape influence signatures of specific cell types, we selected tumor cells and macrophages—the most abundant cell types, which together cover ~65% of our cell population (Figure S8D). Hierarchical clustering of the shape influence signatures showed distinct clustering patterns between these cell types, indicating that prediction of the same protein expression can be influenced by different shape features in tumor cells versus macrophages (Figure S8E). Notable differences include PD-L1 clustering with proliferation markers in tumor cells but with inflammatory proteins in macrophages, suggesting cell type-specific shape requirements for immune checkpoint function.<sup>33,34</sup> Additionally, in tumor cells, the proliferation proteins Ki67 and phospho-S6 and the immune evasion proteins PD-L1 and IDO clustered together, while the structural proteins vimentin with beta-catenin formed a distinct cluster. In contrast, in macrophages, the structural protein vimentin and the inflammatory protein myeloperoxidase (MPO) grouped together, while the immune activation markers CD68 and HLA-DR had very distinct shape influence signatures compared with CD11c and CD209. This interpretability approach could be extended to other cell types to systematically explore how cellular shape influences protein expression. Identifying proteins that have a unique shape signature, or shape signatures that are similar to those of other

proteins, provides phenotypic information that may be relevant for better understanding protein function. Altogether, these results suggest that cell shape importance is associated with protein function and thus may be used to generate hypotheses about potential protein functions, which could be particularly useful for proteins with unknown or poorly characterized functions.

### Tumor cell shape is associated with p53 expression

We next used the same approach to measure more specifically the contribution of cell shape to the prediction of protein expression in the context of cell type. For each pair of (cell type, protein), we measured the residual variability in the protein’s expression within the cell type that is explained by cell shape (Figure 2A). Namely, averaged across patients, for every pair of (cell type, protein), we constructed the  $\Delta$ adjusted  $R^2$  matrix, where for each bin ( $i, j$ ) we calculated the contribution of shape to the prediction of the expression of the specific protein  $i$  in the context of cell type  $j$ . This  $\Delta$ adjusted  $R^2$  matrix encoded 16 (cell types)  $\times$  36 (proteins) = 576 such relations, enabling us to screen for shape-dependent proteins in the context of their cell type (Figure 2B). Expectedly, cell shape contributed to the prediction of the expression levels of dsDNA and histones (HEK9ac, HEK2me3), presumably reflecting coordinated changes in both cell shape and histone content during the cell cycle.<sup>35,36</sup> Next, we examined the contribution of cell shape to the expression of p53 in tumor cells. We decided to concentrate on p53 due to its pivotal role as a tumor suppressor gene and its high mutation rate in TNBC.<sup>37</sup> p53 mutations are frequently observed in many types of cancers, including TNBC, and the protein plays a role in regulating cell cycle arrest, apoptosis, and senescence in response to various cellular stresses.<sup>38</sup> Heterogeneity in p53 expression within tumor cell subpopulations<sup>39</sup> has been speculated to influence their behavior and response to therapy.<sup>40</sup> In the context of TNBC, p53 mutations are highly prevalent, with mutation rates reaching up to 80%,<sup>41</sup> often leading to the accumulation of nonfunctional p53 and contributing to the aggressive nature and poor prognosis of TNBC.<sup>42</sup> Here, we revealed an association linking high expression of p53 in tumor cells and cell shape (Figure 2B). This association between p53 and tumor cell shape was visually and statistically evident in some patients, as demonstrated by a separation in the two-dimensional principal component analysis (PCA)-reduced shape space when comparing p53-positive and p53-negative (as defined in<sup>18</sup>) cells (Figures 2C and S9). Visual observation (Figure 2C, right) and quantification (Figure 2D) showed that p53-positive cells were larger than p53-negative cells, suggesting the existence of a p53-expression-dependent subpopulation with distinct size signatures. We confirmed this association in an independent cohort of patients with TNBC from a different clinic, acquired by a different lab using a different technology (imaging mass cytometry, IMC)<sup>43</sup> (STAR Methods) (Figure 2E). Finally, we

(D–F) Spearman correlation scores between a cell’s p53 expression and its area across different patients (each represented by a data point), derived from a MIBI-TOF TNBC ( $n = 40$  patients) (D), IMC TNBC ( $n = 58$  patients) (E), and CODEX CRC ( $n = 35$  patients) (F) cohorts. All panels exhibited a similar pattern, with data points above 0 indicating a positive correlation between p53 expression and cell size. For all panels, one sample  $t$  test  $p$  values were  $< 0.0001$ , suggesting strong evidence against the null hypothesis of no correlation. For visualization purposes, one outlier patient was discarded from the IMC TNBC dataset. Boxes represent the interquartile range (25th–75th percentile); whiskers extend to  $1.5 \times$  the IQR; and individual data points are overlaid as dots. See also Figures S8 and S9.

revealed that this size-associated p53 expression in tumor cells was also apparent in a cohort of patients with CRC.<sup>24</sup> (Figure 2F). Overall, we suggest that p53 expression in tumor cells is associated with increased cell size across a variety of cancers.

### Cell shape contributes to graph neural network-based clinical prediction

Our results indicate that cell shape features contribute to the quantitative description of protein expression within TNBC tissues but can it contribute to better characterization of disease state? To investigate the potential contribution of shape features to the prediction of clinical outcomes, we defined a graph classification problem (see STAR Methods). Specifically, we constructed an undirected network graph based on the image data, as outlined in,<sup>17</sup> where each cell represented a node, with its protein expression as the node's attributes. The network was then fed into a graph convolutional network (GCN), which is a specialized type of neural network designed to work directly with graph structures<sup>44</sup> (Figure 3A). The GCN operates by propagating information between connected nodes in the graph, effectively enabling each node to “gather” information from its neighboring nodes. This process allows the network to learn both local and global patterns in the data. Each layer in the GCN captures increasing levels of neighborhood information, enabling nodes to “communicate” with nodes farther away in the graph. Previous studies have shown that this approach could predict clinical outcomes, with cohorts in the order of dozens of patients.<sup>17</sup>

We demonstrated that GCNs could predict disease state from tissue sections' single-cell networks for three cohorts (MIBI-TOF TNBC, IMC TNBC, and CODEX HNC) and for multiple clinical readouts (Figures 3B, 3C, and S10). To evaluate the contribution of cell shape to clinical outcome prediction, we compared the performance of two models: 1) a baseline GCN model as described above and 2) the baseline model with the inclusion of single-cell shape as a conditioning factor. The shape-aware GCN models surpassed their corresponding baseline models in predicting a total of 8 out of 9 different clinical readouts from these three datasets (Figures 3B, 3C, and S10). These results indicate that single-cell shape encodes complementary discriminative information regarding disease state, beyond protein expression and cellular spatial composition.

### DISCUSSION

Using disease-related human tissue sections, we systematically investigated the bi-directional link between a cell's shape and its protein expression in the context of multiple cell types, diseases, and disease states. Cell shape is precisely regulated by a combination of intracellular and extracellular cues, can control cell signaling, is indicative of a cell's physiological state, and its dysregulation can be linked to disease progression stage.<sup>4,6,7,9,20,45–63</sup> Accordingly, cell shape is a key readout for pathological diagnosis and treatment decisions, and one of the most studied readouts in the broad domain of cell biology. Until recently, the ability to systematically study the relationships between cell shape and gene expression was restricted to population averages of cell line models.<sup>3</sup> The recent emergence of spatial multiplexed single-

cell imaging technologies enabled us to quantitatively study the intricate relationships between the shape of single cells and their protein expression within a more physiologically relevant context of heterogeneous cell populations in their native state in intact tissue samples *in situ*. Specifically, using machine learning performance as our metric, we established that some of the within-cell type protein expression variability can be explained by a cell's shape and some of the within-cell type cell shape variability can be explained by a cell's protein expression. These associations between cell shape and protein expression seem to be universal across cohorts of four different diseases (TNBC, TB, CRC, and HNC) acquired using two technologies (MIBI-TOF, CODEX) and were amplified for cell state markers.

We demonstrate multiple applications where integration of cell shape can contribute to downstream analyses of spatial multiplexed single-cell imaging data. First, identification of cell subtypes and cell states. We showed that the contribution of cell shape to protein expression prediction can unbiasedly screen all matched cell-type and protein pairs. In the context of TNBC, such a screen identified (in one cohort) and then confirmed (in another cohort) an enrichment of p53 expression in larger tumor cells, a subpopulation that was also identified in a CRC cohort. Second, generation of insights regarding potential protein functionalities. We showed that the interpretation of the most prominent shape features for the prediction of protein expression uncovered shape signatures that clustered according to protein function, highlighting the potential of using shape-based representations to generate hypotheses regarding protein function. Third, enhancement of clinical outcome prediction. We showed that inclusion of shape features mildly but consistently enhanced GCN-based clinical outcome predictions across three cohorts for 8 out of 9 different clinical readouts.

The terms cell “shape” and “morphology” are sometimes used interchangeably but have distinct meanings. Cell morphology includes cell shape but encompasses a broader set of measurements that encode a richer representation of the cell state. Morphological readouts can include information regarding intracellular organization and intercellular context beyond that encoded in cell shape, for example metabolic and proteomic components, by implicitly extracting this information from raw image texture. In the context of spatial multiplexed technologies, cell morphology has been shown to assist in mapping 7-to-40-plex CODEX at single-cell resolution,<sup>21</sup> in cell type classification.<sup>64</sup> The downside of cell morphology is that it is more difficult to biologically interpret and thus it is harder to extract specific biologically meaningful insights. Cell shape is widely studied and can be more easily interpreted (e.g., larger p53-positive tumor cells), validated, and linked to specific molecular players (e.g., Jones et al.<sup>65</sup>) and thus was the focus of our study.

The prediction performance gain attributed to cell shape was consistent for the vast majority of patients in all diseases and across all models but moderate in magnitude. A similar performance gain was recently reported for the contribution of the cell's microenvironment to the prediction of single-cell protein expression beyond cell type.<sup>16</sup> One reason for this modest effect is that cell type is the most dominant factor in explaining variability in protein expression, especially in current panels that

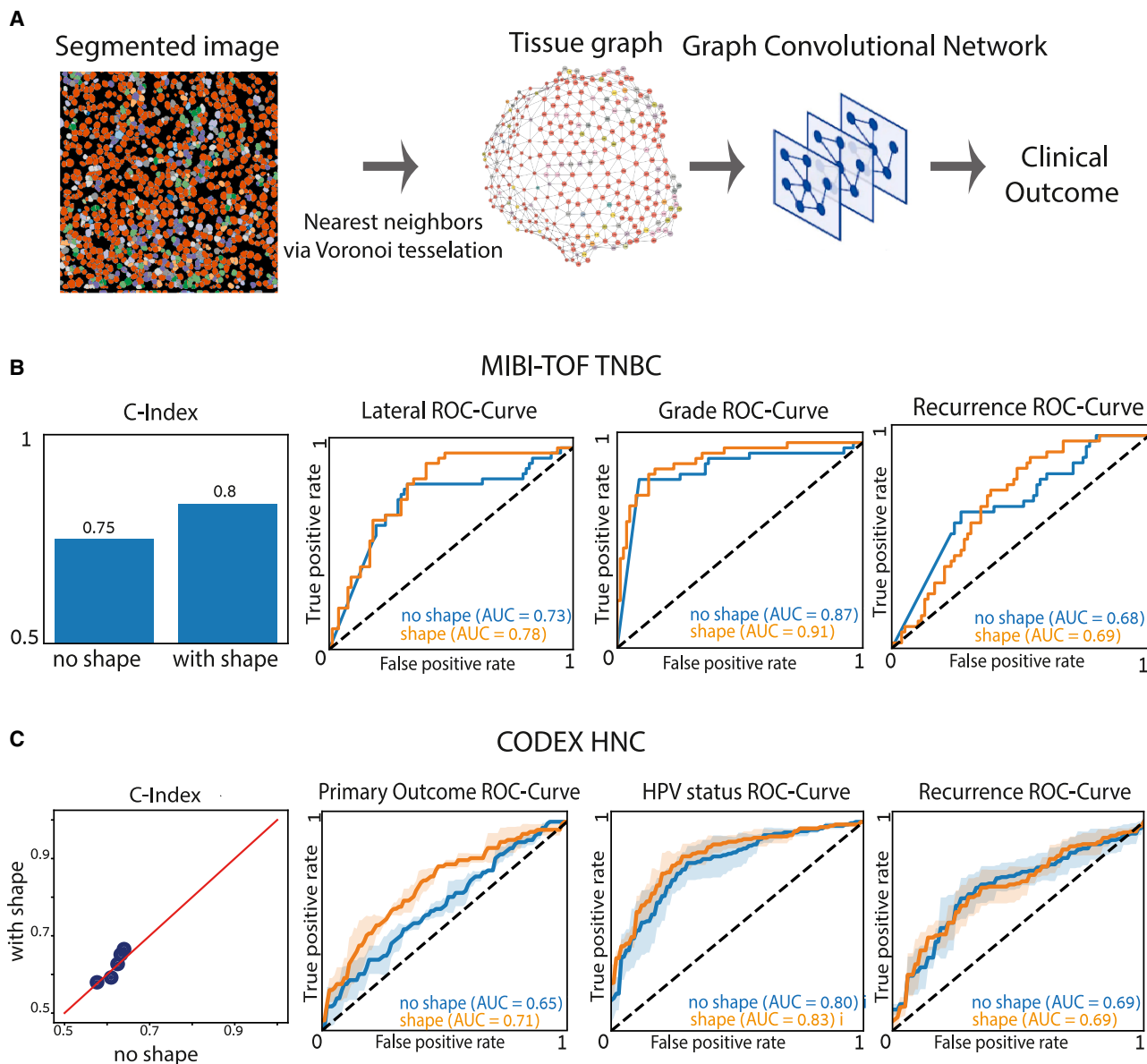


**Figure 3. Cell-shape contribution to the prediction of patients' clinical outcome**

(A) Computational pipeline (left to right): (1) input: cell segmentation and cell type classification; (2) cell adjacency network (aka "graph"): cells are nodes and Delaunay neighbors define edges; node features are defined as the cells' protein expression with or without shape features; and (3) graph convolutional network maps the graph to learn the outcome clinical label.

(B and C) Cell shape contributes to prediction of clinical outcome. The receiver operating characteristic (ROC) curves compare the performance of shape-aware models (orange) and shape-independent models (blue). Shape-aware GCNs led to an improvement in most clinical prediction tasks. (B) TNBC cohort ( $n = 40$  patients), clinical outcome (left to right): C-index: lifespan post-diagnosis (survival ranking metric); lateral: edge of the tissue (binary measure); grade: tumor aggressiveness level (multiclass); and recurrence: returning cancer (binary measure). For grade, the micro-average ROC (weighted average) is presented due to highly imbalanced classes. Due to the limited number of patients, the models were evaluated using a leave-one-out strategy, where each sample was iteratively held out as a test set while the remaining samples were used for training. (C) Head and neck (HNC) ( $n = 139$  patients), clinical outcomes (left to right): C-index: lifespan post-diagnosis (survival ranking metric); primary outcome: head and neck squamous cell carcinomas (HNSCC) (positive or negative); HPV status: presence of human papillomavirus (binary); and recurrence: returning cancer (binary). The models were evaluated using 5-fold cross-validation. In the C-index scatterplot (left), each data point represents one of the 5-fold cross-validation scores of shape-aware ( $y$  axis) and baseline ( $x$  axis) predictions. Data points above the diagonal  $y = x$  indicate that the corresponding shape-aware model yields more accurate predictions. ROC curves (right) show the mean (solid line) and standard deviation (shaded area) of the shape-aware (orange) and baseline (blue) model performance.

See also [Figure S10](#).

are limited to a few dozen proteins, where most are used to infer cell type. Technological advancements are expected to increase the number of proteins, enabling larger numbers of “cell state” markers that we expect to have higher associations with cell shape.<sup>66,67</sup> Another reason for the moderate contribution of cell shape is the low spatial resolution. Physical pixel sizes of 0.4–1  $\mu\text{m}$ , which are standard in spatial multiplexed technologies, are limiting (even perfect) cell segmentation to a rough outline. This is probably the main reason behind our failure to predict cell type from cell shape. However, we argue that the ability to consistently measure the contribution of cell shape across a variety of applications and datasets indicates a strong biological signal that goes beyond the noise levels introduced by coarse segmentation. For clinical outcome predictions, these cell shape features are routinely extracted during standard segmentation preprocessing. By incorporating them, we enhance the predictive power of clinical models without requiring additional experiments or data acquisition costs. In clinical stratification, such as predicting treatment response, a 3% gain in Area under the ROC curve (AUC) can be the deciding factor in correctly identifying patients in borderline diagnostic categories. Indeed, high-resolution and 3D cell shapes provide discriminative information regarding the cell’s microenvironment,<sup>46,59</sup> molecular organization,<sup>9,68</sup> and treatment.<sup>69</sup> Future technologies with improved resolution and 3D information will likely amplify these gains, enabling the application of more powerful shape descriptors and enhanced discrimination between different cell states.

### Limitations of the study

Several limitations should be considered when interpreting the results of this study. First, the contribution of cell shape to the prediction of protein expression, while consistent across patients and diseases, is moderate in magnitude, reflecting the dominance of cell type as the primary source of variability in current protein panels. Second, the spatial resolution of the multiplexed imaging technologies used in this study (0.4–1  $\mu\text{m}$  per pixel) restricts cell shape features to coarse outlines, limiting the discriminative power of shape descriptors. Higher-resolution and three-dimensional imaging technologies may reveal stronger associations. Third, current protein panels are biased toward lineage markers selected for cell type classification and include relatively few cell state markers; panels with more cell state markers may show stronger shape-expression associations. Fourth, cell segmentation quality inherently affects shape feature extraction; although our sensitivity analyses demonstrate robustness to moderate segmentation noise, systematic errors in segmentation could influence the results. Finally, our study focuses on cell shape rather than the broader cell morphology, which may encode additional information from intracellular organization and image texture that is not captured by the shape features used here.

### RESOURCE AVAILABILITY

#### Lead contact

Further information and requests for resources should be directed to and will be fulfilled by the lead contact, Assaf Zaritsky ([assafzar@gmail.com](mailto:assafzar@gmail.com)).

### Materials availability

This study did not generate new materials.

### Data and code availability

- The following datasets are publicly available: MIBI-TNBC,<sup>18</sup> MIBI-TB,<sup>23</sup> CODEX-HNC,<sup>17</sup> CODEX-CRC,<sup>24</sup> and IMC-TNBC.<sup>43</sup> The MIBI-Melanoma dataset will be publicly available upon journal publication<sup>25</sup> and, until then, is available upon request from the [lead contact](#). The specific sources and accession information for each dataset are detailed in the [STAR Methods](#).
- Source code for all analyses is publicly available at <https://github.com/zaritskiy/shape-exp-modeling> and archived at Zenodo: <https://doi.org/10.5281/zenodo.19593915>.
- Any additional information required to reanalyze the data reported in this paper is available from the [lead contact](#) upon request.

### ACKNOWLEDGMENTS

This research was supported by the Wellcome Leap Delta Tissue program (to A.Z., L.S., and M.P.), by the Wellcome Trust’s Bioimaging Technology Development Award (to A.Z. and M.P.), and by the Israel Science Foundation (ISF, grant no. 2516/21 to A.Z.). L.K. holds the Fred and Andrea Fallek President’s Development Chair. She is supported by the Enoch Foundation Research Fund, the Rising Tide Foundation, the Sharon Levine Foundation, the Rosettes Foundation, and grants funded by the Dwek Center for Cancer Immunotherapy, the European Research Council (948811), the Israel Science Foundation (2481/20 and 3830/21) within the Israel Precision Medicine Partnership program, and the Melanoma Research Alliance Team Science Award (1200724).

### AUTHOR CONTRIBUTIONS

A.Z. and L.K. conceived the study. Y.T. developed the computational methods. Y.T., L.K., and A.Z. analyzed and interpreted the results. Y.T., O.K.-G., and A.Z. drafted the manuscript. Y.B. and C.O. generated data. L.L. and G.T. preprocessed data. A.Z., L.K., M.P., and L.S. acquired funding and mentored Y.T., Y.B., C.O., L.L., G.T., and L.A.R. All authors edited the manuscript and approved its content.

### DECLARATION OF INTERESTS

The authors declare no competing interests.

### DECLARATION OF GENERATIVE AI AND AI-ASSISTED TECHNOLOGIES IN THE WRITING PROCESS

During the preparation of this work, the authors used ChatGPT (OpenAI), Claude (Anthropic), and Gemini (Google) for text editing. After using these tools, the authors reviewed and edited the content as needed and take full responsibility for the content of the publication.

### STAR★METHODS

Detailed methods are provided in the online version of this paper and include the following:

- [KEY RESOURCES TABLE](#)
- [EXPERIMENTAL MODEL AND STUDY PARTICIPANT DETAILS](#)
  - Datasets
  - Triple-negative breast cancer MIBI-TOF (MIBI-TNBC)
  - Tuberculosis MIBI-TOF (MIBI-TB)
  - HNC CODEX (CODEX-HNC)
  - Collateral cancer CODEX (CODEX-CRC)
  - Triple-negative breast cancer IMC (IMC-TNBC)
  - Melanoma MIBI-TOF (MIBI-Melanoma)
- [METHOD DETAILS](#)
  - Single-cell shape features

- Associating cell shape to cell type
- Machine-learning models
- Baseline model
- Prior-aware model
- Patient-aware model
- Patient- and prior-aware model
- Microenvironment-aware model
- Microenvironment- and prior-aware model
- Measuring machine-learning models' performance with the adjusted R2 measurement
- Assessing sensitivity to spatial resolution and to segmentation errors
- Dimensionality reduction
- Feature importance analysis (explainability)
- Constructing the spatial multicellular network (graph)
- Graph convolutional network
- Models' optimization and evaluation
- **QUANTIFICATION AND STATISTICAL ANALYSIS**
  - Statistical analysis

### SUPPLEMENTAL INFORMATION

Supplemental information can be found online at <https://doi.org/10.1016/j.crmeth.2026.101463>.

Received: June 8, 2025

Revised: March 2, 2026

Accepted: April 24, 2026

### REFERENCES

1. Mogilner, A., and Keren, K. (2009). The Shape of Motile Cells. *Curr. Biol.* *19*, R762–R771. <https://doi.org/10.1016/j.cub.2009.06.053>.
2. Mostafa, H.K.K. (2022). Different Cells of the Human Body: Categories and Morphological Characters. *J. Microsc. Ultrastruct.* *10*, 40–46. [https://doi.org/10.4103/jmau.jmau\\_74\\_20](https://doi.org/10.4103/jmau.jmau_74_20).
3. Haghighi, M., Caicedo, J.C., Cimini, B.A., Carpenter, A.E., and Singh, S. (2022). High-dimensional gene expression and morphology profiles of cells across 28,000 genetic and chemical perturbations. *Nat. Methods* *19*, 1550–1557. <https://doi.org/10.1038/s41592-022-01667-0>.
4. Bakal, C., Aach, J., Church, G., and Perrimon, N. (2007). Quantitative Morphological Signatures Define Local Signaling Networks Regulating Cell Morphology. *Science* *316*, 1753–1756. <https://doi.org/10.1126/science.1140324>.
5. Clark, A.G., and Paluch, E. (2011). Mechanics and Regulation of Cell Shape During the Cell Cycle. In *Cell Cycle in Development Results and Problems in Cell Differentiation*, J.Z. Kubiak, ed. (Springer Berlin Heidelberg), pp. 31–73. [https://doi.org/10.1007/978-3-642-19065-0\\_3](https://doi.org/10.1007/978-3-642-19065-0_3).
6. Keren, K., Pincus, Z., Allen, G.M., Barnhart, E.L., Marriott, G., Mogilner, A., and Theriot, J.A. (2008). Mechanism of shape determination in motile cells. *Nature* *453*, 475–480. <https://doi.org/10.1038/nature06952>.
7. Wu, P.-H., Gilkes, D.M., Phillip, J.M., Narkar, A., Cheng, T.W.-T., Marchand, J., Lee, M.-H., Li, R., and Wirtz, D. (2020). Single-cell morphology encodes metastatic potential. *Sci. Adv.* *6*, eaaw6938. <https://doi.org/10.1126/sciadv.aaw6938>.
8. Pincus, Z., and Theriot, J.A. (2007). Comparison of quantitative methods for cell-shape analysis. *J. Microsc.* *227*, 140–156. <https://doi.org/10.1111/j.1365-2818.2007.01799.x>.
9. Viana, M.P., Chen, J., Knijnenburg, T.A., Vasan, R., Yan, C., Arakaki, J.E., Bailey, M., Berry, B., Borensztein, A., Brown, E.M., et al. (2023). Integrated intracellular organization and its variations in human iPSC cells. *Nature* *613*, 345–354. <https://doi.org/10.1038/s41586-022-05563-7>.
10. Nassiri, I., and McCall, M.N. (2018). Systematic exploration of cell morphological phenotypes associated with a transcriptomic query. *Nucleic Acids Res.* *46*, e116. <https://doi.org/10.1093/nar/gky626>.
11. Neumann, B., Walter, T., Hériché, J.-K., Bulkescher, J., Erfle, H., Conrad, C., Rogers, P., Poser, I., Held, M., Liebel, U., et al. (2010). Phenotypic profiling of the human genome by time-lapse microscopy reveals cell division genes. *Nature* *464*, 721–727. <https://doi.org/10.1038/nature08869>.
12. Caicedo, J.C., Cooper, S., Heigwer, F., Warchal, S., Qiu, P., Molnar, C., Vasilevich, A.S., Barry, J.D., Bansal, H.S., Kraus, O., et al. (2017). Data-analysis strategies for image-based cell profiling. *Nat. Methods* *14*, 849–863. <https://doi.org/10.1038/nmeth.4397>.
13. Chandrasekaran, S.N., Ceulemans, H., Boyd, J.D., and Carpenter, A.E. (2021). Image-based profiling for drug discovery: due for a machine-learning upgrade? *Nat. Rev. Drug Discov.* *20*, 145–159. <https://doi.org/10.1038/s41573-020-00117-w>.
14. Keren, L., Bosse, M., Thompson, S., Risom, T., Vijayaragavan, K., McCaffrey, E., Marquez, D., Angoshtari, R., Greenwald, N.F., Fienberg, H., et al. (2019). MIBI-TOF: A multiplexed imaging platform relates cellular phenotypes and tissue structure. *Sci. Adv.* *5*, eaax5851. <https://doi.org/10.1126/sciadv.aax5851>.
15. Black, S., Phillips, D., Hickey, J.W., Kennedy-Darling, J., Venkatarraaman, V.G., Samusik, N., Goltsev, Y., Schürch, C.M., and Nolan, G.P. (2021). CODEX multiplexed tissue imaging with DNA-conjugated antibodies. *Nat. Protoc.* *16*, 3802–3835. <https://doi.org/10.1038/s41596-021-00556-8>.
16. Fischer, D.S., Schaar, A.C., and Theis, F.J. (2023). Modeling intercellular communication in tissues using spatial graphs of cells. *Nat. Biotechnol.* *41*, 332–336. <https://doi.org/10.1038/s41587-022-01467-z>.
17. Wu, Z., Trevino, A.E., Wu, E., Swanson, K., Kim, H.J., D'Angio, H.B., Preska, R., Charville, G.W., Dalerba, P.D., Egloff, A.M., et al. (2022). Graph deep learning for the characterization of tumour microenvironments from spatial protein profiles in tissue specimens. *Nat. Biomed. Eng.* *6*, 1435–1448. <https://doi.org/10.1038/s41551-022-00951-w>.
18. Keren, L., Bosse, M., Marquez, D., Angoshtari, R., Jain, S., Varma, S., Yang, S.-R., Kurian, A., Van Valen, D., West, R., et al. (2018). A Structured Tumor-Immune Microenvironment in Triple Negative Breast Cancer Revealed by Multiplexed Ion Beam Imaging. *Cell* *174*, 1373–1387.e19. <https://doi.org/10.1016/j.cell.2018.08.039>.
19. Van Valen, D.A., Kudo, T., Lane, K.M., Macklin, D.N., Quach, N.T., DeFelice, M.M., Maayan, I., Tanouchi, Y., Ashley, E.A., and Covert, M.W. (2016). Deep Learning Automates the Quantitative Analysis of Individual Cells in Live-Cell Imaging Experiments. *PLoS Comput. Biol.* *12*, e1005177. <https://doi.org/10.1371/journal.pcbi.1005177>.
20. Gut, G., Herrmann, M.D., and Pelkmans, L. (2018). Multiplexed protein maps link subcellular organization to cellular states. *Science* *361*, eaar7042. <https://doi.org/10.1126/science.aar7042>.
21. Wu, E., Trevino, A.E., Wu, Z., Swanson, K., Kim, H.J., D'Angio, H.B., Preska, R., Chiou, A.E., Charville, G.W., Dalerba, P., et al. (2023). *7-UP*: Generating in silico CODEX from a small set of immunofluorescence markers. *PNAS Nexus* *2*, pgad171. <https://doi.org/10.1093/pnasnexus/pgad171>.
22. Alizadeh, E., Castle, J., Quirk, A., Taylor, C.D.L., Xu, W., and Prasad, A. (2020). Cellular morphological features are predictive markers of cancer cell state. *Comput. Biol. Med.* *126*, 104044. <https://doi.org/10.1016/j.combiomed.2020.104044>.
23. McCaffrey, E.F., Donato, M., Keren, L., Chen, Z., Delmastro, A., Fitzpatrick, M.B., Gupta, S., Greenwald, N.F., Baranski, A., Graf, W., et al. (2022). The immunoregulatory landscape of human tuberculosis granulomas. *Nat. Immunol.* *23*, 318–329. <https://doi.org/10.1038/s41590-021-01121-x>.
24. Schürch, C.M., Bhatte, S.S., Barlow, G.L., Phillips, D.J., Noti, L., Zlobec, I., Chu, P., Black, S., Demeter, J., Mcllwain, D.R., et al. (2020). Coordinated Cellular Neighborhoods Orchestrate Antitumoral Immunity at the

- Colorectal Cancer Invasive Front. *Cell* 182, 1341–1359.e19. <https://doi.org/10.1016/j.cell.2020.07.005>.
25. Amitay, Y., Milo, I., Keidar Haran, T., Deis, S., Truzman, G., Elhanani, O., Salame, T.-M., Azimov, M., Stein, I., Cohen, J.E., et al. (2024). Immune organization in sentinel lymph nodes of melanoma patients is prognostic of distant metastases. Preprint at *Cancer Biology*. <https://doi.org/10.1101/2024.11.24.625041>.
26. Lundberg, S., and Lee, S.-I. (2017). A Unified Approach to Interpreting Model Predictions. *Advances in Neural Information Processing Systems* 30, 4765–4774. <https://doi.org/10.48550/arXiv.1705.07874>.
27. Baraks, G., Tseng, R., Pan, C.-H., Kasliwal, S., Leiton, C.V., Shroyer, K.R., and Escobar-Hoyos, L.F. (2022). Dissecting the Oncogenic Roles of Keratin 17 in the Hallmarks of Cancer. *Cancer Res.* 82, 1159–1166. <https://doi.org/10.1158/0008-5472.CAN-21-2522>.
28. Maeda, T., Nakanishi, Y., Hirofani, Y., Fuchinoue, F., Enomoto, K., Sakurai, K., Amano, S., and Nemoto, N. (2016). Immunohistochemical co-expression status of cytokeratin 5/6, androgen receptor, and p53 as prognostic factors of adjuvant chemotherapy for triple negative breast cancer. *Med. Mol. Morphol.* 49, 11–21. <https://doi.org/10.1007/s00795-015-0109-0>.
29. Menz, A., Gorbokon, N., Viehweger, F., Lennartz, M., Hube-Magg, C., Hornsteiner, L., Kluth, M., Völkel, C., Luebke, A.M., Fraune, C., et al. (2023). Pan-keratin Immunostaining in Human Tumors: A Tissue Microarray Study of 15,940 Tumors. *Int. J. Surg. Pathol.* 31, 927–938. <https://doi.org/10.1177/10668969221117243>.
30. Weeks, S.E., Kammerud, S.C., Metge, B.J., AlSheikh, H.A., Schneider, D.A., Chen, D., Wei, S., Mobley, J.A., Ojesina, A.I., Shevde, L.A., and Samant, R.S. (2021). Inhibiting  $\beta$ -catenin disables nucleolar functions in triple-negative breast cancer. *Cell Death Dis.* 12, 242. <https://doi.org/10.1038/s41419-021-03531-z>.
31. Sun, X., and Kaufman, P.D. (2018). Ki-67: more than a proliferation marker. *Chromosoma* 127, 175–186. <https://doi.org/10.1007/s00412-018-0659-8>.
32. Igolkina, A.A., Zinkevich, A., Karandasheva, K.O., Popov, A.A., Selifanova, M.V., Nikolaeva, D., Tkachev, V., Penzar, D., Nikitin, D.M., and Buzdin, A. (2019). H3K4me3, H3K9ac, H3K27ac, H3K27me3 and H3K9me3 Histone Tags Suggest Distinct Regulatory Evolution of Open and Condensed Chromatin Landmarks. *Cells* 8, 1034. <https://doi.org/10.3390/cells8091034>.
33. Tang, Q., Chen, Y., Li, X., Long, S., Shi, Y., Yu, Y., Wu, W., Han, L., and Wang, S. (2022). The role of PD-1/PD-L1 and application of immune-checkpoint inhibitors in human cancers. *Front. Immunol.* 13, 964442. <https://doi.org/10.3389/fimmu.2022.964442>.
34. Huo, G., Liu, W., Zhang, S., and Chen, P. (2023). Efficacy of PD-1/PD-L1 Plus CTLA-4 Inhibitors in Solid Tumors Based on Clinical Characteristics: a Meta-Analysis. *Immunotherapy* 15, 189–207. <https://doi.org/10.2217/imt-2022-0140>.
35. Nagao, Y., Sakamoto, M., Chinen, T., Okada, Y., and Takao, D. (2020). Robust classification of cell cycle phase and biological feature extraction by image-based deep learning. *Mol. Biol. Cell* 31, 1346–1354. <https://doi.org/10.1091/mbc.E20-03-0187>.
36. Roukos, V., Pegoraro, G., Voss, T.C., and Misteli, T. (2015). Cell cycle staging of individual cells by fluorescence microscopy. *Nat. Protoc.* 10, 334–348. <https://doi.org/10.1038/nprot.2015.016>.
37. Duffy, M.J., Synnott, N.C., O'Grady, S., and Crown, J. (2022). Targeting p53 for the treatment of cancer. *Semin. Cancer Biol.* 79, 58–67. <https://doi.org/10.1016/j.semcancer.2020.07.005>.
38. Hafner, A., Bulyk, M.L., Jambhekar, A., and Lahav, G. (2019). The multiple mechanisms that regulate p53 activity and cell fate. *Nat. Rev. Mol. Cell Biol.* 20, 199–210. <https://doi.org/10.1038/s41580-019-0110-x>.
39. Yang, P., Du, C.W., Kwan, M., Liang, S.X., and Zhang, G.J. (2013). The impact of p53 in predicting clinical outcome of breast cancer patients with visceral metastasis. *Sci. Rep.* 3, 2246. <https://doi.org/10.1038/srep02246>.
40. Li, N., Lorenzi, F., Kalakouti, E., Normatova, M., Babaei-Jadidi, R., Tomlinson, I., and Nateri, A.S. (2015). FBXW7-mutated colorectal cancer cells exhibit aberrant expression of phosphorylated-p53 at Serine-15. *Oncotarget* 6, 9240–9256. <https://doi.org/10.18632/oncotarget.3284>.
41. Cancer Genome Atlas Network (2012). Comprehensive molecular portraits of human breast tumours. *Nature* 490, 61–70. <https://doi.org/10.1038/nature11412>.
42. Bianchini, G., Balko, J.M., Mayer, I.A., Sanders, M.E., and Gianni, L. (2016). Triple-negative breast cancer: challenges and opportunities of a heterogeneous disease. *Nat. Rev. Clin. Oncol.* 13, 674–690. <https://doi.org/10.1038/nrclinonc.2016.66>.
43. Luque, L.M., Khan, A., Torrisi, G., Green, T.D., Hardman, D., Owczarek, C., Phillips, T.A., Marks, D.S., Parsons, M., Sander, C., et al. (2026). Identifying tissue states by spatial protein patterns related to chemotherapy response in triple-negative breast cancer. *eLife* 15, RP109177. <https://doi.org/10.7554/eLife.109177>.
44. Kipf, T.N., and Welling, M. (2017). Semi-Supervised Classification with Graph Convolutional. 5th International Conference on Learning Representations (ICLR). <https://doi.org/10.48550/ARXIV.1609.02907>.
45. Cachoux, V.M.L., Balakireva, M., Gracia, M., Bosveld, F., López-Gay, J.M., Maugarny, A., Gaugué, I., Di Pietro, F., Rigaud, S.U., Noiret, L., et al. (2023). Epithelial apoptotic pattern emerges from global and local regulation by cell apical area. *Curr. Biol.* 33, 4807–4826.e6. <https://doi.org/10.1016/j.cub.2023.09.049>.
46. Dent, L.G., Curry, N., Sparks, H., Bousgouni, V., Maioli, V., Kumar, S., Munro, I., Butera, F., Jones, I., Arias-Garcia, M., et al. (2024). Environmentally dependent and independent control of 3D cell shape. *Cell Rep.* 43, 114016. <https://doi.org/10.1016/j.celrep.2024.114016>.
47. Driscoll, M.K., Welf, E.S., Jamieson, A.R., Dean, K.M., Isogai, T., Fiolka, R., and Danuser, G. (2019). Robust and automated detection of subcellular morphological motifs in 3D microscopy images. *Nat. Methods* 16, 1037–1044. <https://doi.org/10.1038/s41592-019-0539-z>.
48. Goudarzi, M., Tarbashevich, K., Mildner, K., Begemann, I., Garcia, J., Paksa, A., Reichman-Fried, M., Mahabaleshwar, H., Blaser, H., Hartwig, J., et al. (2017). Bleb Expansion in Migrating Cells Depends on Supply of Membrane from Cell Surface Invaginations. *Dev. Cell* 43, 577–587.e5. <https://doi.org/10.1016/j.devcel.2017.10.030>.
49. Haftbaradaran Esfahani, P., and Knöll, R. (2020). Cell shape: effects on gene expression and signaling. *Biophys. Rev.* 12, 895–901. <https://doi.org/10.1007/s12551-020-00722-4>.
50. Kai, F., Laklai, H., and Weaver, V.M. (2016). Force Matters: Biomechanical Regulation of Cell Invasion and Migration in Disease. *Trends Cell Biol.* 26, 486–497. <https://doi.org/10.1016/j.tcb.2016.03.007>.
51. Lamouille, S., Xu, J., and Derynck, R. (2014). Molecular mechanisms of epithelial–mesenchymal transition. *Nat. Rev. Mol. Cell Biol.* 15, 178–196. <https://doi.org/10.1038/nrm3758>.
52. Marshall, W.F. (2020). Pattern Formation and Complexity in Single Cells. *Curr. Biol.* 30, R544–R552. <https://doi.org/10.1016/j.cub.2020.04.011>.
53. McBeath, R., Pirone, D.M., Nelson, C.M., Bhadriraju, K., and Chen, C.S. (2004). Cell Shape, Cytoskeletal Tension, and RhoA Regulate Stem Cell Lineage Commitment. *Dev. Cell* 6, 483–495. [https://doi.org/10.1016/S1534-5807\(04\)00075-9](https://doi.org/10.1016/S1534-5807(04)00075-9).
54. Meyers, J., Craig, J., and Odde, D.J. (2006). Potential for Control of Signaling Pathways via Cell Size and Shape. *Curr. Biol.* 16, 1685–1693. <https://doi.org/10.1016/j.cub.2006.07.056>.
55. Mills, J.C., Stone, N.L., Erhardt, J., and Pittman, R.N. (1998). Apoptotic Membrane Blebbing Is Regulated by Myosin Light Chain Phosphorylation. *J. Cell Biol.* 140, 627–636. <https://doi.org/10.1083/jcb.140.3.627>.
56. Qu, F., Guilak, F., and Mauck, R.L. (2019). Cell migration: implications for repair and regeneration in joint disease. *Nat. Rev. Rheumatol.* 15, 167–179. <https://doi.org/10.1038/s41584-018-0151-0>.
57. Rohban, M.H., Singh, S., Wu, X., Berthet, J.B., Bray, M.-A., Shrestha, Y., Varelas, X., Boehm, J.S., and Carpenter, A.E. (2017). Systematic

- morphological profiling of human gene and allele function via Cell Painting. *eLife* 6, e24060. <https://doi.org/10.7554/eLife.24060>.
58. Sailem, H.Z., and Bakal, C. (2017). Identification of clinically predictive metagenes that encode components of a network coupling cell shape to transcription by image-omics. *Genome Res.* 27, 196–207. <https://doi.org/10.1101/gr.202028.115>.
59. Segal, D., Mazloom-Farsibaf, H., Chang, B.-J., Roudot, P., Rajendran, D., Daetwyler, S., Fiolka, R., Warren, M., Amatruda, J.F., and Danuser, G. (2022). In vivo 3D profiling of site-specific human cancer cell morphotypes in zebrafish. *J. Cell Biol.* 221, e202109100. <https://doi.org/10.1083/jcb.202109100>.
60. Tee, S.-Y., Fu, J., Chen, C.S., and Janmey, P.A. (2011). Cell Shape and Substrate Rigidity Both Regulate Cell Stiffness. *Biophys. J.* 100, L25–L27. <https://doi.org/10.1016/j.bpj.2010.12.3744>.
61. Weems, A.D., Welf, E.S., Driscoll, M.K., Zhou, F.Y., Mazloom-Farsibaf, H., Chang, B.-J., Murali, V.S., Gihana, G.M., Weiss, B.G., Chi, J., et al. (2023). Blebs promote cell survival by assembling oncogenic signalling hubs. *Nature* 615, 517–525. <https://doi.org/10.1038/s41586-023-05758-6>.
62. Yanagida, A., Corujo-Simon, E., Revell, C.K., Sahu, P., Stirparo, G.G., Aspalter, I.M., Winkel, A.K., Peters, R., De Belly, H., Cassani, D.A.D., et al. (2022). Cell surface fluctuations regulate early embryonic lineage sorting. *Cell* 185, 777–793.e20. <https://doi.org/10.1016/j.cell.2022.01.022>.
63. Yin, Z., Sadok, A., Sailem, H., McCarthy, A., Xia, X., Li, F., Garcia, M.A., Evans, L., Barr, A.R., Perrimon, N., et al. (2013). A screen for morphological complexity identifies regulators of switch-like transitions between discrete cell shapes. *Nat. Cell Biol.* 15, 860–871. <https://doi.org/10.1038/ncb2764>.
64. Amitay, Y., Bussi, Y., Feinstein, B., Bagon, S., Milo, I., and Keren, L. (2023). CellSighter: a neural network to classify cells in highly multiplexed images. *Nat. Commun.* 14, 4302. <https://doi.org/10.1038/s41467-023-40066-7>.
65. Jones, I., Arias-Garcia, M., Pascual-Vargas, P., Beykou, M., Dent, L., Chaudhuri, T.P., Roumeliotis, T., Choudhary, J., Sero, J., and Bakal, C. (2024). Coupling of Nuclear Translocation to Cell Size Promotes Robustness to Fluctuations in YAP/TAZ Concentration. *Molecular Omics* 20, 554–569. <https://doi.org/10.1039/d4mo00051j>.
66. Liu, C.C., Greenwald, N.F., Kong, A., McCaffrey, E.F., Leow, K.X., Mrdjen, D., Cannon, B.J., Rumberger, J.L., Varra, S.R., and Angelo, M. (2023). Robust phenotyping of highly multiplexed tissue imaging data using pixel-level clustering. *Nat. Commun.* 14, 4618. <https://doi.org/10.1038/s41467-023-40068-5>.
67. Scheuermann, S., Kristmann, B., Engelmann, F., Nuernbergk, A., Scheuermann, D., Koloseus, M., Abed, T., Solass, W., and Seitz, C.M. (2024). Unveiling spatial complexity in solid tumor immune microenvironments through multiplexed imaging. *Front. Immunol.* 15, 1383932. <https://doi.org/10.3389/fimmu.2024.1383932>.
68. Mazloom-Farsibaf, H., Zou, Q., Hsieh, R., Danuser, G., and Driscoll, M.K. (2023). Cellular harmonics for the morphology-invariant analysis of molecular organization at the cell surface. *Nat. Comput. Sci.* 3, 777–788. <https://doi.org/10.1038/s43588-023-00512-4>.
69. De Vries, M., Dent, L., Curry, N., Rowe-Brown, L., Bousgouni, V., Tyson, A., Dunsby, C., and Bakal, C. (2022). 3D single-cell shape analysis using geometric deep learning. Preprint at Bioinformatics. <https://doi.org/10.1101/2022.06.17.496550>.
70. Carpenter, A.E., Jones, T.R., Lamprecht, M.R., Clarke, C., Kang, I.H., Friman, O., Guertin, D.A., Chang, J.H., Lindquist, R.A., Moffat, J., et al. (2006). CellProfiler: image analysis software for identifying and quantifying cell phenotypes. *Genome Biol.* 7, R100. <https://doi.org/10.1186/gb-2006-7-10-r100>.

## STAR★METHODS

### KEY RESOURCES TABLE

REAGENT or RESOURCE	SOURCE	IDENTIFIER
<b>Deposited data</b>		
MIBI-TOF TNBC dataset (40 patients, 36 proteins)	Keren et al. <sup>18</sup>	<a href="https://mibi-share.ionpath.com">https://mibi-share.ionpath.com</a>
MIBI-TOF TB dataset (17 patients, 38 proteins)	McCaffrey et al. <sup>23</sup>	Mendeley Data: <a href="https://doi.org/10.26434/chemrxiv-2023-03-01">dr5fkgrtb6</a>
CODEX HNC dataset (139 patients, 22 proteins)	Wu et al. <sup>17</sup>	Zenodo: <a href="https://zenodo.org/record/13179600">13179600</a>
CODEX CRC dataset (35 patients, 56 proteins)	Schürch et al. <sup>24</sup>	TCIA: <a href="https://doi.org/10.7937/TCIA.2020.FQN0-0326">https://doi.org/10.7937/TCIA.2020.FQN0-0326</a>
MIBI-TOF Melanoma dataset (69 patients, 36 proteins)	Amitay et al. <sup>25</sup>	N/A
IMC TNBC dataset (58 patients, 35 proteins)	Luque et al. <sup>69</sup>	Biolmage Archive: <a href="https://doi.org/10.6019/S-BIAD2027">https://doi.org/10.6019/S-BIAD2027</a>
<b>Software and algorithms</b>		
Source code and test data	This paper	GitHub: <a href="https://github.com/zaritskylab/shape-exp-modeling">https://github.com/zaritskylab/shape-exp-modeling</a> ; Zenodo: <a href="https://doi.org/10.5281/zenodo.19593915">https://doi.org/10.5281/zenodo.19593915</a>

## EXPERIMENTAL MODEL AND STUDY PARTICIPANT DETAILS

### Datasets

We analyzed five public and one new dataset (Table S3).

### Triple-negative breast cancer MIBI-TOF (MIBI-TNBC)

We reused an existing MIBI-TOF TNBC dataset that included 40 patients.<sup>18</sup> 36 proteins were used to identify 16 cell types across 178,366 cells, with physical pixel size of  $0.5 \times 0.5 \mu\text{m}^2$ . We used the same cell types annotations (Tumor, Endothelial, Mesenchyme, Tregs, CD4 T cells, CD8 T cells, CD3 T cells, NK cells, B cells, Neutrophils, Macrophages, DC, DC/Mono, Mono/Neu, Immune other), and the same segmentation masks from.<sup>18</sup> Clinical readouts include lifespan post-diagnosis, lateral (i.e., sample taken from the edge of the tissue, binary), grade (tumor aggressiveness level), and recurrence (binary).

### Tuberculosis MIBI-TOF (MIBI-TB)

We reused an existing MIBI-TOF TB granulomas dataset that included 26 patients.<sup>23</sup> 38 proteins were used to identify 19 cell types across 56,402 cells, with physical pixel size of  $0.5 \times 0.5 \mu\text{m}^2$ . We used the same cell type annotations (endothelial, CD16\_CD14\_Mono, CD8\_T, CD4\_T, imm\_other, CD14\_Mono, neutrophil, fibroblast, B\_cell, CD68\_Mac, CD206\_Mac, CD11c\_DC/Mono, CD11b/c\_CD206\_Mac/Mono, mast, CD163\_Mac, Treg, and epithelial) and the same segmentation masks from.<sup>23</sup>

### HNC CODEX (CODEX-HNC)

We reused an existing CODEX HNC dataset that included 139 patients.<sup>17</sup> 22 proteins were used to identify 16 cell types across 2,061,162 cells, with physical pixel size of  $0.4 \times 0.4 \mu\text{m}^2$ . We used the same cell type annotations (Tumor (Podo+), Tumor (CD20<sup>+</sup>), CD4 T cell, Tumor (Ki67+), Stromal/Fibroblast, Tumor (CD21<sup>+</sup>), Naive immune cell, Macrophage, B cell, Tumor, APC, Lymph vessel, CD8 T cell, Vessel, Granulocyte, Tumor (CD15<sup>+</sup>)) and the same segmentation masks from.<sup>17</sup> Clinical readouts include: lifespan post-diagnosis, primary outcome (HNSCC positive or negative), HPV status (i.e., presence of human papillomavirus, binary), recurrence (binary).

### Collateral cancer CODEX (CODEX-CRC)

We reused an existing CODEX Colorectal cancer (CRC) dataset that included 35 patients.<sup>24</sup> 56 proteins were used to identify 16 cell types across 218,372 cells, with physical pixel size of  $0.4 \times 0.4 \mu\text{m}^2$ . We used the same cell type annotations (B cell, CD4T, CD8T, CD3T, Treg, DC, Fibroblast, Tumor, Macrophage, Neuron, Neutrophil, Plasma, Stroma, Endothelial, SMV, and Lymphatic) and the same segmentation masks from.<sup>24</sup>

### Triple-negative breast cancer IMC (IMC-TNBC)

We reused an existing IMC TNBC dataset that included 58 patients.<sup>43</sup> 35 proteins were used to identify 32 cell types across 3,738,846 cells, with a physical pixel size of  $1 \times 1 \mu\text{m}^2$ . We used the same cell type annotations (Exhausted T cell, Immune/Cancer, Th1 T helper, CAF, NK cell (FOXP3), Monocyte (Tbet), GB Active T cell, Macrophage, T cell, B7H4+ Cancer (CD11b), Unassigned, Endothelial, Monocytes, Memory T cell, Monocyte (HLA), B/T/NK cell, CD44<sup>+</sup> MAC, B7H4+ Cancer, Vim+ Cancer/NK, Mem CD8 T cell, Cancer stem cell, Antigen-presenting cell, Reg T cell, Cytotoxic T cell, E-Cad cancer, FOXP3+ Cancer, NK cells/Cancer, T/B cells, PanCK Cancer, B-cell, Alfa-SMA+ Monocytes, and T cell/Cancer) and the same segmentation masks from.<sup>43</sup>

### Melanoma MIBI-TOF (MIBI-Melanoma)

We reused an existing MIBI-TOF melanoma dataset that included 69 patients (multiple ROIs per patient),<sup>25</sup> that will be publicly available upon journal publication, and until then will be available upon request from the [lead contact](#). 36 proteins were used to identify 27 cell types across 1,701,560 cells, with a physical pixel size of  $0.5 \times 0.5 \mu\text{m}^2$ . We used the same cell type annotations (CD4 T cell, CD4 Treg, CD4 APC, Tfh%CD4 CD4 T cell, CD45RA + MHC2+, IDO1+ DCs, IDO1+CCR7+ DCs, CD14<sup>+</sup>CD11c+ DCs, CD14<sup>+</sup>CD11c+CD209+ DCs, Germinal center cell, B cell, CD45RA + CD4<sup>+</sup> T cell, CD8 T cell, CD163 Mac, CD209 Mac, CD206 Mac, CD68 Mac, Mono CD14 DR, Neutrophil, NK cell, DCs, HEVs, Vessels, Stroma, Collagen, Unidentified, Tumor) and the same segmentation masks from.<sup>25</sup>

## METHOD DETAILS

### Single-cell shape features

We used python's skimage library (region props function) to extract 12 typical shape features for each cell's segmentation mask<sup>66,70</sup> (Table S1).

### Associating cell shape to cell type

To overcome the confounding effect of inter-patient variability we compared the shape features distributions within each patient. First, for every cell type and for every shape feature we calculated the mean shape feature value per patient. Second, for each feature  $f$  and for each pair of cell types  $(X, Y)$ , we tested the null hypothesis that the mean value of feature  $f$  in cell type  $X$  is the same as the mean value of feature  $f$  in cell type  $Y$ , using matched pairs of observations from the same patient. In other words, the null hypothesis states that the probability of an observation from cell type  $X$  being greater than an observation from cell type  $Y$

$$P(X_{\{f,i\}} > Y_{\{f,i\}}) = P(Y_{\{f,i\}} > X_{\{f,i\}}),$$

where  $i$  denotes the patient from which the matched observations (i.e., mean value of feature  $f$ ) are drawn. We applied the Wilcoxon sign-rank test with FDR corrections for every triplet consisting of two cell types and a feature  $(X, Y, f)$  and examined pairs consisting of a cell type and a feature that were the largest/smallest among the other cell types.

We measured the coefficient of variation (CoV) in the cell area as a measure for heterogeneity. The CoV is defined as the ratio between an observable standard deviation to its mean in a given population, where larger CoV values indicate higher variability.

To systematically and quantitatively explore more complex associations between cell type and cell shape we turned to using machine learning as a relative measurement metric. We used the single cell shape features to train an XGBoost machine learning classifiers to classify cells according to their types. Models were trained to predict a cell-type from its (i) shape features, (ii) protein expression or (iii) both protein expression and shape features with an 80-20% train-test split.

### Machine-learning models

For all our deep learning models, i.e., Deep Neural Network (DNN) and Graph Convolutional Networks (GCN) we used python's pytorch and pytorch geometric libraries. For linear models we used scikit-learn linear models (LinearRegression, Ridge and Lasso). 3-fold cross validation was performed with the DNN, and 5-fold cross validation was performed with the GCN. In each fold, a different subset of the cells was chosen randomly for the test.

### Baseline model

A three-layer DNN  $f_{\text{baseline}}$  was trained to predict a cell's target  $y \in \mathbb{R}^m$  from its one-hot encoded cell-type vector  $x_{\text{cell}} \in \{0, 1\}^n$ .  $n$  represents the number of cell types, and  $m$  signifies the dimensions of the target. The learned model parameters are noted as  $\theta$ . The model function is given by  $f_{\text{baseline}}(x_{\text{cell}}; \theta) = y$ . Note that the baseline model predicts a continuous target (protein expression or shape, Figure 1) from a discrete input (cell type) and thus loses the within-cell type heterogeneity. Thus, we expect the prediction to be close to the mean of the cell type class's target.

### Prior-aware model

Prior-aware models enhance  $f_{\text{baseline}}$  by incorporating prior features (shape or protein expression). Denoted by  $x_{\text{prior}} \in \mathbb{R}^p$ , the prior is concatenated to the one-hot encoded cell-type vector  $x_{\text{cell}} \in \{0, 1\}^n$ . Here,  $p$  represents the prior features dimensions ( $p = 12$  for cell shape, e.g.,  $p = 36$  for the MIBI-TNBC data). The model function is given by  $f_{\text{baseline+prior}}(x_{\text{cell}} || x_{\text{prior}}; \theta) = y$ .

### Patient-aware model

Patient-aware model enhances  $f_{baseline}$  by incorporating patient ID identifier  $x_{patient} \in \{0, 1\}^b$  alongside the one-hot encoded cell-type vector  $x_{cell} \in \{0, 1\}^n$ , aiming to capture patient-specific variation in the target (protein expression or shape). Here,  $b$  represents the number of patients. The model function is given by:  $f_{batch}(x_{cell} \| x_{patient}; \theta) = y$ .

### Patient- and prior-aware model

Combines  $x_{cell} \in \{0, 1\}^n$ ,  $x_{patient} \in \{0, 1\}^b$  and  $x_{prior} \in \mathbb{R}^p$ . The model function is given by:  $f_{batch+prior}(x_{cell} \| x_{patient} \| x_{prior}; \theta) = y$

### Microenvironment-aware model

Following the work of Fischer et al.,<sup>16</sup> the microenvironment-aware models input is composed of  $x_{cell} \in \{0, 1\}^n$ ,  $x_{patient} \in \{0, 1\}^b$ , and a binary microenvironment representation  $x_{microenvironment} \in \{0, 1\}^l$ , indicating the presence of each cell type within a fixed radius of 70  $\mu\text{m}$  around the target cell.  $l$  is the number of cell types, and the binary digit indicates whether the specific cell type is within the specified radius, without considering the number of cells. This model integrates spatial context to predict the target. The microenvironment-aware model function is given by:  $f_{microenvironment}(x_{cell} \| x_{patient} \| x_{microenvironment}; \theta) = y$ .

### Microenvironment- and prior-aware model

Combines  $x_{cell} \in \{0, 1\}^n$ ,  $x_{patient} \in \{0, 1\}^b$ ,  $x_{prior} \in \mathbb{R}^p$ , and  $x_{microenvironment} \in \{0, 1\}^l$ . The model function is given by:  $f_{microenvironment+prior}(x_{cell} \| x_{patient} \| x_{prior} \| x_{microenvironment}; \theta) = y$ . Note that in all models, the prior is either cell shape, or cell protein expression, and the target is either protein expression or cell shape, accordingly, depending on the model configuration (Figure 1).

### Measuring machine-learning models' performance with the adjusted R<sup>2</sup> measurement

We use the adjusted-R<sup>2</sup> as a metric to assess our machine learning models' performance. R<sup>2</sup> measures the variance explained by the model, in our manuscript, the protein expression/shape variance across all cells. R<sup>2</sup> = 0 implies that the model is no better than simply predicting the mean of the target values. R<sup>2</sup> < 0 implies that the model performs worse than predicting the mean (i.e., explains less variance than a trivial baseline), and correspondingly R<sup>2</sup> > 0 implies that the model performs better than predicting the mean (i.e., it explains less variance than a trivial baseline).

In our manuscript, we decided to use the adjusted-R<sup>2</sup> measure because it is a more appropriate measure to compare models that were trained with different numbers of variables. Consistent positive adjusted-R<sup>2</sup> across patients implies that the model learned a relation between the cell's shape to the protein expression or vice versa. Importantly, most of the variance in protein expression is dominated by cell type - a prior that is incorporated in the baseline model. Thus, showing that cell shape/protein expression can consistently explain some of the remaining within cell-type variance ( $\Delta R^2 > 0$ ) establish a link between cell shape to protein expression and/or from protein expression to cell shape beyond the within cell type variability.

### Assessing sensitivity to spatial resolution and to segmentation errors

To systematically quantify the sensitivity of the contribution of cell shape to the prediction of protein expression to the quality of the cell's segmentation we performed two analyses. First, to assess the effect of reduced resolution, we downsampled the segmentation masks by a factor of 0.8 and 0.5 and assessed the deterioration of the shape-to-protein contribution. Second, to assess the effect of segmentation errors we gradually introduced measurement noise to the (segmentation-derived) cell shape measurements and assessed the deterioration of the shape-to-protein contribution. More specifically, we added Gaussian noise with mean 0 and a standard deviation equal to each feature's standard deviation multiplied by the specified noise level to the single cell shape measurements. For example, if the noise level was 10%, we multiply the feature's standard deviation by 0.1 to determine the standard deviation of the noise. We repeated this procedure for noise levels of 10%, 30%, and 50%, and then evaluated how these increasing levels of noise affected the contribution of cell shape to the prediction of protein expression. Both analyses relied on the segmentations that were included with the published datasets because applying different segmentation algorithms will require the re-execution of the entire analysis pipeline, including laborious cell type annotations according to the new segmentation masks. Both analyses referred to the cell type-, patient-, microenvironment-aware model with or without the cell shape information.

### Dimensionality reduction

We used PCA on the shape features for dimensionality reduction.

### Feature importance analysis (explainability)

For AI explainability, we have used python's Captum library, and specifically the GradientSHAP function. GradientSHAP is a gradient method to compute SHAP values, which are based on the Shapley values proposed in cooperative game theory and compute the contribution of each feature to each individual prediction.<sup>26</sup> To cluster the feature importance patterns per protein, we used hierarchical clustering implementation in python's SciPy package with the default settings.

### Constructing the spatial multicellular network (graph)

Each cell represented a node, where cells' centroids (defined as the center of mass from the segmentation masks) established fixed node positions. Spatially adjacent pairs of cells were connected with an edge according to the Delaunay triangulation. Specifically, we used SciPy's 'Delaunay' function followed by 'vertex\_neighbor\_vertices' attribute to construct the edges, excluding those defined between cells more than 100  $\mu\text{m}$  apart. The nodes' positions, along with spatial adjacency, defined a graph structure that was identical for both baseline and shape-aware models. Protein expression served as the primary node attributes; for the shape-aware models, cell shape features were concatenated to these attribute vectors and did not alter the graph structure, the cell centroids, or any inter-cellular distances.

### Graph convolutional network

In this model we perform a whole graph classification task to predict the clinical outcome, using a 3 layers graph convolutional network (GCN). For this purpose, each tissue section was transformed to an undirected graph, where cells defined the nodes and Delaunay neighbors defined the edges. There was no distance threshold to the edge definition to avoid sub-graphs, long-distance edges were rare. For the baseline GCN model, the protein expression of each cell defines the node attributes (Figure 3A). In the shape-aware GCN model, we concatenate the shape features vector to the cell type attributes. To perform a whole graph classification task we aggregated the information across nodes after the final layer, using global max pooling, to a single value of the clinical outcome. We used leave-one-out cross validation for TNBC, and 5-fold cross validation for HNC. The area under the Receiver Operating Characteristic (ROC) curve was used to compare the performance of models without versus with the shape priors. For the grade label in the MIBI-TNBC cohort, the data was imbalanced, thus we used micro-averaged ROC (i.e., weighted-average). Area under the ROC curve (AUC) was used as the measure of discrimination. Note that all prediction scores across each leave-out-out model were pooled for this analysis. This analysis reports a lower bound because different models can produce different scores.

### Models' optimization and evaluation

The DNN and the GCN models were optimized using the Adam optimizer.

In all equations below,  $Y_i$  is the  $k$ -dimensional ground truth vector for a given cell,  $\hat{Y}_i$  is the  $k$ -dimensional prediction for a given cell,  $\bar{Y}$  is the per-dimension mean,  $N$  is the number of cells,  $M$  is the classes,  $k$  is the dimension of the ground truth and prediction vectors. The measures can be calculated per patient, or across the entire dataset.

For regression models, we used the mean squared error (MSE) loss:

$$L_{MSE}(Y, \hat{Y}) = \frac{1}{N} \sum_{i=1}^N (y_i - \hat{y}_i)^2$$

and performance was evaluated with the coefficient of determination

$$R^2 : R^2 = 1 - \frac{\sum_{i=1}^N (Y_i - \hat{Y}_i)^2}{\sum_{i=1}^N (Y_i - \bar{Y})^2}.$$

For classification models, we used the cross-entropy (CE) loss:

$$L_{CE}(Y, \hat{Y}) = - \sum_{c=1}^M y_{i,c} \log(\hat{y}_{i,c})$$

and performance was evaluated with the F1 score:

$$F1 = 2 \times \frac{\text{precision} \times \text{recall}}{\text{precision} + \text{recall}}.$$

## QUANTIFICATION AND STATISTICAL ANALYSIS

### Statistical analysis

The non-parametric Wilcoxon signed-rank test was used for statistical analysis testing the null hypothesis that a distribution of the differences between the adjusted  $R^2$  scores of patients with versus without the shape/protein priors was distributed around zero. One sample  $t$  test was used in other cases.